Climate forcing and response to greenhouse gases, aerosols and ozone in CESM1

Climate forcing and response to greenhouse gases, aerosols and ozone in CESM1

Alcide Zhao[1*], David S. Stevenson[1] and Massimo A. Bollasina[1]

[1]School of GeoSciences, University of Edinburgh, Edinburgh, UK

[*]Corresponding author: Alcide Zhao (alcide.zhao@ed.ac.uk)

Key Points:

- Once in equilibrium, both the global mean temperature and precipitation responses are twice as large as the transient 1970-2010 changes.
- The temperature response per unit forcing varies significantly across many factors, and should be used carefully for short-lived species.
- Changes in daily precipitation distribution are dominated by greenhouse gases at global scale, but by aerosol changes at regional scales.

Abstract

It is crucial to reduce uncertainties in our understanding of the climate impacts of short-lived climate forcers (SLCFs), in the context that their emissions/concentrations are anticipated to decrease significantly in the coming decades worldwide. Using the Community Earth System Model (CESM1), we performed time-slice experiments to investigate the effective radiative forcing (ERF) and climate responses to 1970-2010 changes in well-mixed greenhouse gases, anthropogenic aerosols, as well as tropospheric and stratospheric ozone. Once the present-day climate has fully responded to 1970-2010 changes in all forcings, both the global mean temperature and precipitation responses are twice as large as the transient ones, with wet regions getting wetter, and dry regions drier. The temperature response per unit ERF for short-lived species varies considerably across many factors including forcing agents, and the magnitudes and locations of emission changes. This suggests that the ERF should be used

This article has been accepted for publication and undergone full peer review but has not been through the copyediting, typesetting, pagination and proofreading process which may lead to differences between this version and the Version of Record. Please cite this article as doi: 10.1029/2019JD030769

carefully to interpret the climate impacts of SLCFs. Changes in both the mean and the probability distribution of global mean daily precipitation are driven mainly by GHG increases. However, changes in the frequency distributions of regional mean daily precipitation are more strongly influenced by changes in aerosols, rather than greenhouse gases. This is particularly true over Asia and Europe where aerosol changes have significant impacts on the frequency of heavy-to-extreme precipitation. Our results may help guide more reliable near-future climate projections and allow us to manage climate risks more effectively.

1 Introduction

It is well established that human activities have altered the chemical and physical properties of the atmosphere (Acosta Navarro et al., 2017), and therefore influenced the climate system (Schmidt et al., 2014). Changes in many climate features, especially the global warming trend, have been shown to be driven mainly by the increasing abundance of well-mixed greenhouse gases (GHGs) (Stocker et al., 2013). However, there are also significant concerns about the impacts of short-lived (i.e., having a shorter lifetime than CO_2) climate forcers (SLCFs, notably aerosols and ozone and their precursor gases) on both air quality and climate (Stocker et al., 2013; Schmale et al., 2014; Stohl et al., 2015). Unlike GHGs, concentrations of SLCFs depend strongly on the geographical location of emission sources, and their radiative forcings are largely heterogeneous and uncertain (Stohl et al., 2015; Aamaas et al., 2017). More importantly, the climate response to SLCFs differs from that of quasi-uniform forcing agents at regional scales (Lamarque et al., 2011; Aamaas et al., 2017; Zhao et al., 2018; Zhao et al., 2019).

The climate system evolves slowly in response to changing emissions: once a perturbation (radiative forcing) is introduced, the climate system will respond and adjust to

restore the radiative balance on decadal timescales, and even centennial timescales when accounting for the deep ocean heat uptake (Yang and Zhu, 2011). The climate in the new equilibrium can be very different from its transient state as the latter does not account for the full long-term response to the imposed forcing (Yoshimori et al., 2016). The equilibrium climate response to GHGs, and CO_2 in particular, has received much attention (Marvel et al., 2016; Rugenstein and Bloch-Johnson, 2016; Yoshimori et al., 2016; Caldwell et al., 2018). In comparison, there are fewer studies on the equilibrium climate response to changes in SLCFs, except some looking at idealized experiments where emissions/concentrations of aerosols are scaled rather arbitrarily (Kühn et al., 2014; Liu et al., 2018; Persad and Caldeira, 2018; Samset et al., 2018). However, despite their short lifetimes, a major fraction of SLCFs' impacts are associated with the slow response of the ocean through adjustments in circulation and clouds (Allen and Sherwood, 2011; Ganguly et al., 2012; Voigt et al., 2017; Wang et al., 2017). The slow response emerges on decadal to centennial timescales (Ganguly et al., 2012; Voigt et al., 2017; Wang et al., 2017) even after these SLCFs are removed. For example, equilibrium model simulations indicate that the long-term slow response is more important in shaping the total equilibrium response of the Asian monsoon to aerosol forcing (Ganguly et al., 2012; Wang et al., 2017). That is, similar to these long-lived species such as CO_2, the climate impacts of SLCFs will not be fully realised until the climate has equilibrated, suggesting the importance of studying the equilibrium climate responses to SLCFs as GHGs. Some studies compared the differences in climate responses between GHGs and aerosols using mixed-layer ocean models (Feichter et al., 2004; Ming and Ramaswamy, 2009; Ocko et al., 2014; Dallafior et al., 2016; Hodnebrog et al., 2016; Chen and Dong, 2018; Tian et al., 2018). Nevertheless, to our knowledge, there are very few studies (e.g., Wang et al. (2018a)) specifically designed to systematically compare the equilibrium climate response to recent changes in major climate drivers (e.g., GHGs, aerosols and ozone) using a (or a set of) fully-

coupled climate model(s). Also, the difference between equilibrium and transient climate responses have not been investigated so far. However, the evolving climate response, and consequently the equilibrium sensitivity, of SLCFs is of scientific interest, as they show significant new insights into how the climate system responds to SLCFs, and that there are important differences between SLCFs and GHGs. This provides useful implications for future long-term climate projection and policy-making in the context that we expect significant changes in future emissions of SLCFs. Here we focus on the 1970-2010 period for the following reasons. Firstly, a very large fraction of the preindustrial to present-day global warming occurred after about 1970 (Stocker et al., 2013). Secondly, emissions of CO_2 started to increase in a dramatic way since the 1970s (Olivier et al., 2005; Figueres et al., 2018). Thirdly and most importantly, as described below, the atmospheric abundance of aerosols and ozone have undergone very dramatic and distinctive changes since around 1970.

While Asia is currently the dominant emission source of air pollutants worldwide, Europe and North America have been the primary emission sources for more than a century since industrialization (Lamarque et al., 2010; Smith et al., 2011). The first continental air quality directive was implemented in Europe in 1970, while country-level air quality acts have been introduced even earlier (the mid-1960s). Since then legislation has been gradually introduced in industrialized regions in order to reduce the impacts of acid rain and air pollution (Crippa et al., 2016). As a result, air pollutant emissions followed contrasting trends between developed and developing countries during the past few decades. For example, SO_2 emissions from developing countries (e.g., China and India) increased steadily beginning in the 1950s while emissions from developed regions started to decline after around 1970 (Smith et al., 2011). Only after about 2010 have some developing countries started to take mitigation measures. For instance, Chinese SO_2 emissions have been declining since about

2012; as a consequence, India was recently reported to have overtaken China as the largest present-day emitter of SO_2 (Li et al., 2017).

Aerosols represent the largest uncertainty in the radiative forcing on climate since the preindustrial era (Boucher et al., 2013). For example, the Intergovernmental Panel on Climate Change (IPCC) Fifth Assessment Report (AR5) estimates a 1750-2011 aerosol effective radiative forcing (ERF) of -0.9 W m^{-2}, but with a large uncertainty range from -1.9 to -0.1 W m^{-2} (Myhre et al., 2013). Such uncertainties originate from compounding uncertainties in emissions sources, aerosol composition, size distribution, spatial and temporal distribution, and the multiple ways through which they affect climate. Aerosols can influence climate by absorbing/scattering mainly shortwave radiation (the direct effects), and by modifying cloud microphysical properties and therefore cloud albedo and lifetime (aerosol-cloud interactions or indirect effects). These, in combination, modulate precipitation in different and competing ways (Andreae and Rosenfeld, 2008; Fan et al., 2016; Zhao et al., 2018).

In addition to changes in the trends of emissions of air pollutants between developed and developing regions during the past few decades, there are also distinct changes in tropospheric and stratospheric ozone during 1970-2010. More specifically, tropospheric ozone concentration has increased since the pre-industrial era due to increases in precursor emissions (Stevenson et al., 2013; Checa-Garcia et al., 2018), and varies inter-annually due to fluctuations in downward transport of stratospheric ozone (Hsu and Prather, 2009; Monks et al., 2015; Xie et al., 2016). Simultaneously, industrial emissions of halocarbons have led to widespread depletion of the stratospheric ozone layer since at least the 1970s (Solomon, 1999). Thanks to the Montreal Protocol and its amendments stratospheric ozone has started to recover but at a much slower rate (~3 times slower than the depletion) after about 2000 (Solomon et al., 2016; Hossaini et al., 2017; Kuttippurath and Nair, 2017; Wilmouth et al., 2017). Ozone modulates solar radiation and has a different surface impact depending on its

location: stratospheric ozone depletion reduces UV absorption, cools the stratosphere, and warms the surface, while tropospheric ozone has a greenhouse effect that warms the surface and the lower atmosphere (Stevenson et al., 2013; Xie et al., 2016). The 1850-2014 total ozone ERF is estimated to be +0.30 W m^{-2}, primarily from changes in tropospheric ozone increase (+0.33 W m^{-2}) and, in a minor way, from stratospheric ozone depletion (-0.03 W m^{-2}) (Checa-Garcia et al., 2018).

The arguments above indicate the particularity and importance of studying the period 1970-2010. This allows us to examine the differences and relative roles of very distinctive changes in individual forcing agents (especially GHGs versus SLCFs) during recent decades. These are significant for interpreting and attributing currently observed climate change. More importantly, we attempt to improve our understanding of how far present-day climate is from a steady-state with the current level of emissions, which is critical to better constrain long-term climate projections and more adequately prepare for future climate-related risks. Model and simulations, as well as analysis methods, are described in Section 2. The climate response, in particular, changes in temperature and precipitation, and the differences between transient and equilibrium responses, are presented in Section 3, followed by a summary in Section 4.

2 Methods

We make use of the fully-coupled Community Earth System Model (CESM1; Hurrell et al. (2013)) at a horizontal resolution of 0.9°×1.25° and 1°×1° in the atmosphere and ocean, respectively. The atmosphere component of CESM1 is the Community Atmosphere Model 5 (CAM5). CAM5 prescribes the concentrations of CO_2 and CH_4 with seasonal cycles and latitudinal gradients (Conley et al., 2012). CAM5 includes a three-mode (Aitken, accumulation, and coarse) aerosol scheme (Modal Aerosol Module 3). Several aerosol

species (sulphate, organic carbon (OC), black carbon (BC), sea-salt, and dust) are simulated and their number concentrations and mass are prognostically calculated. Simple gas-phase chemistry is included for sulphur species. That is, SO_2 is converted into SO_4 through both gas-phase OH oxidation and aqueous-phase oxidation by H_2O_2 and O_3 (Liu et al., 2015; Tilmes et al., 2015). BC is emitted into the accumulation mode and ages, which allows it to be coated with soluble species (e.g., SO_4) and to nucleate cloud droplets (Conley et al., 2012; Liu et al., 2012).

Anthropogenic aerosols and their precursor emissions are from the Emissions Database for Global Atmospheric Research (EDGAR) version 4.3.2 inventory for the years 1970 and 2010 (Crippa et al., 2016). The EDGAR aerosol emissions are mapped to conform to the CAM5 emission protocol following Lamarque et al. (2010). GHGs, natural aerosols and other reactive gas emissions/concentrations are from Lamarque et al. (2010) for 1970 and Lamarque et al. (2011) for 2010. Ozone concentrations for 1970 and 2010 (See Figure S1 in the supporting information for the zonal mean distribution of 1970-2010 ozone changes) are from WACCM simulations (Marsh et al., 2013), as used by the CESM1 large ensemble experiment (LENS; Kay et al. (2015)). The LENS was designed to disentangle the signal of climate change from the underlying internal climate variability using the same CESM1 model setup as used here. It has a set of 30 ensemble member of historical (1920-2005) and future (2006-2100, following the RCP8.5 scenario) all-forcing simulations (Riahi et al., 2007; Van Vuuren et al., 2011). Each of the ensemble members has the same forcing and only differs by being initialised from randomly perturbed atmospheric conditions (Kay et al., 2015).

Using CESM1, we carried out two baseline experiments branching off from the LENS transient historical simulation at either 1970 or 2010 (See caption of Figure 1 for more details). The baseline simulations were integrated to equilibrium under the 1970 and 2010 all forcings (denoted as B70 and B10). A number of perturbation experiments, branching off

from the LENS transient simulation at 2010, were also performed by alternatively keeping one of the forcing agents at 1970 levels and the others at 2010 levels (see Table 1). For each experiment, a set of paired simulations were performed. The first is with fixed sea surface temperature and sea ice (hereinafter Fsst) fields derived from the LENS transient simulations. The Fsst experiment was integrated for 40 years, with the last 30 years used to diagnose ERF by the difference in the top-of-the-atmosphere (TOA, top of the model in this case) net radiative flux (Forster et al., 2016). The second is under the same forcings as the first one, but with a fully coupled ocean (Fcpd). The Fcpd experiment was integrated into equilibrium after the initial perturbation, with a repeated annual cycle of the forcings. The length of each Fcpd integration is deemed sufficient for analysis once TOA radiation imbalance no longer shows significant trends (less than 5% relative to the mean values stabilizing at ~0.3 W m^{-2}) during the last 30-50 years of each simulation, following recent works (Samset et al.; Samset et al., 2016; Myhre et al., 2017b).

We analyse the last 30 years of each Fcpd simulation (indicated by the black boxes in Figure 1) to show the equilibrium climate responses. Throughout this study, we show differences (Table 1) between 1970 and 2010, to quantify the responses to all forcings (ALL), GHGs, anthropogenic aerosols (AAs), tropospheric ozone increase (Trop. O_3), and stratospheric ozone depletion (Strat. O_3). It must be noted that GHGs refers to those non-ozone GHGs. Following Shindell and Faluvegi (2009), the sensitivity of the surface air temperature responses to local and global radiative forcing is estimated by normalizing area-weighted mean temperature responses against global and regional mean ERF, respectively.

To compare the equilibrium and transient climate responses, we make use of various datasets: output from the LENS for both the historical (1920 – 2005) and future (RCP8.5 for 2006-2100) periods (Kay et al., 2015); monthly mean 2-m temperature from the NCEP/NCAR reanalysis (Kalnay et al., 1996); and monthly observed land-only precipitation

from the Global Precipitation Climatology Centre (GPCC) dataset (Huffman et al., 1997). For above datasets, 15 years of monthly mean fields centred on 1970 and 2010 (7 years either side as reanalysis/observation data are not available beyond 2017) are averaged to produce annual means. The difference between the two 15-year means for 1970 and 2010 from LENS is taken as the transient model response, and those from NCEP/NCAR and GPCC are taken as observational changes.

To produce spatial maps, the analysis is performed on each model grid-box using annual mean values. The statistical significance of the response, as isolated from the corresponding two sets of 30-year runs, is evaluated using the two-tailed Student t-test with a 5% significance level (p-value <0.05), and accounting for serial autocorrelation by adjusting the degrees of freedom following Nychka et al. (2000). For global and regional mean analyses, we first perform an area-weighted mean for each year of each simulation, and then show the results as the mean and 25^{th}-75^{th} percentile spread of the differences between the two sets of 30 year runs.

3. Results

Figure 1 shows the time evolution (annual mean) of the global mean surface air temperature for all model experiments analysed here. Temperature generally increases from the initial condition to reach an approximate equilibrium after ~100 years. The temperature difference between the B70 case in equilibrium and the 1970 initial condition is modest (~0.10 K), indicating that the 1970-2010 equilibrium changes stem primarily from the adjustment to 2010 conditions, while the difference in the initial conditions of the two simulations may also contribute. It is important to point out that the global mean TOA net radiative flux converges from initial values exceeding +1.6 W m^{-2} towards zero as the experiments progress, although even after ~150 years a small imbalance is still left in the last

few decades of the experiments (~0.3 W m^{-2}; see Section 2) due to the large inertia of the deep oceanic circulation which equilibrates on time-scales of several centuries (Yang and Zhu, 2011). This residual forcing will drive additional climate anomalies further to the ones analysed here. Nevertheless, the impacts from the residual forcing are secondary, given the much larger 1970-2010 forcing changes. (Mitchell et al., 1990; Rugenstein and Bloch-Johnson, 2016; Samset et al., 2018).

The 1970-2010 changes in global and regional area-weighted mean anthropogenic aerosol emissions and aerosol burdens, as well as the spatial distribution of the 550-nm aerosol optical depth (AOD), are shown in Figure 2. The anthropogenic aerosol burden and AOD changes shown here are driven primarily (around 90%; Table S1) by emission changes, with the rest attributable to climate change (i.e., changes in meteorology driven mainly by GHG increases). The emissions and burdens of all aerosol species show increasing trends when averaged globally. For example, the global mean sulphate burden has increased by 0.77 mg m^{-2} (~22%). AOD changes are consistent with regional changes in aerosol emissions and burdens, with a striking dipole pattern featuring an AOD increase over Asia and a decrease over Europe and USA.

3.1 Transient versus equilibrium climate responses

To evaluate the performance of CESM1 in simulating transient climate response, we compare the LENS ensemble mean with reanalysis/observations (Figure 3). Further, present-day climate (transient response) is not in equilibrium in response to past emission changes, while the difference between the transient and equilibrium responses is primarily associated with the slow response of the ocean. In order to quantify such differences, we attempt to compare the equilibrium experiments described above with the LENS ensemble mean. The spatial patterns of the 1970-2010 changes in surface air temperature show an overall

agreement across datasets (Figure 3a-c). This is also reflected in the zonal mean profiles (Figure 3d). Comparison between LENS and NCEP/NCAR indicates that apart from the polar regions, the model shows reasonable agreement with reanalysis in reproducing the transient (i.e. LENS) surface air temperature changes. The equilibrium response is roughly double the transient response (Figure 3d), with the global mean 1970-2010 temperature change 0.58 K larger in equilibrium than the transient warming (0.65 K).

Precipitation by nature is more heterogeneous compared to temperature, as is reflected in the spatial patterns of changes (Figure 3e-g). LENS simulated precipitation changes agree in general with the observed ones. However, there are noticeable differences at regional scales such as over equatorial Africa, the Middle East and Southeast Asia. These changes, for example, the wettening over Europe and the drying of the Asian monsoon, as well as the shift of the tropical rain belt, have been broadly discussed in literature as key features of the late-twentieth-century climate evolution (Ropelewski and Halpert, 1987; Bollasina et al., 2011; Hwang et al., 2013; Liu et al., 2013; Acosta Navarro et al., 2017; Jong et al., 2018). The global precipitation pattern displays a striking resemblance between the equilibrium (Figure 3e) and transient (Figure 3f) responses, although the former features anomalies of larger magnitude. The zonal mean (land + ocean) precipitation profile in Figure 3h shows that, compared to the transient response, precipitation increases over the equatorial area (5°S-5°N) and high latitudes but reduces in the mid-latitudes (30°S-5°S and 5°N-40°N) in equilibrium. Globally, the 1970-2010 equilibrium precipitation increase (0.054 mm day^{-1}) is double the transient response (0.026 mm day^{-1}). This is not that surprising given the linkage between changes in precipitation and temperature at global scale.

3.2 Effective radiative forcing and surface air temperature response

The rest of the result section turns to, and focuses on, the ERF and equilibrium climate responses unless otherwise stated. The spatial distribution of TOA ERF and the corresponding surface air temperature responses are shown in Figure 4 (see also Figure S2 for the zonal mean temperature changes). Regional mean ERFs are presented in Figure 5. The global mean 1970-2010 ERF is 1.56±0.45 W m^{-2}, primarily associated with increases in GHGs (1.50±0.44 W m^{-2}) and tropospheric ozone (0.24±0.01 W m^{-2}), and only partially offset by aerosol changes (-0.11±0.14 W m^{-2}) and stratospheric ozone depletion (-0.07±0.15 W m^{-2}). The spatial distribution of ERF associated with GHG increases (Figure 4a) shows substantial uniformity and inter-hemispheric symmetry. In comparison, the ERF associated with aerosol changes (Figure 4b) has larger magnitudes in the NH (where emissions and their changes are the largest), with significant regional differences, and shows a strong anti-correlation with the AOD pattern (Figure 2c). For example, anthropogenic aerosol increases in Asia result in a negative forcing of -1.07±0.91 W m^{-2} (Figure 5d), while aerosol reductions over Europe and USA produce positive forcings of 2.43±0.48 and 1.43±0.88 W m^{-2} (Figure 5e, f) respectively. In addition, the Arctic (Figure 5c) sees a positive aerosol forcing of 0.24±0.42 W m^{-2}, related to European and American aerosol reductions. Tropospheric ozone increase (Figure 4c) and stratospheric ozone depletion (Figure 4d), in general, lead to contrasting forcings. The former generates positive forcing, especially over the NH and with the largest value over the Arctic (0.47±0.31 W m^{-2}). The latter, on the contrary, generates negative forcing, especially over the Southern Hemisphere.

While the spatial patterns of the surface air temperature response (Figure 4e-h) are broadly consistent with the ERF patterns in the corresponding experiments, there are also major dissimilarities. The equilibrium 1970-2010 global mean temperature change, +1.23±0.14 K, is dominated by GHG increases (+1.03±0.16 K). This is also manifested in the

zonal mean changes (Figure S2). The warming from GHGs is notably amplified over the Poles (Figure 4e and S2), and the Arctic in particular, despite a globally homogeneous ERF distribution. The 1970-2010 aerosol changes induce a negative global mean ERF (-0.11±0.14 W m^{-2}), resulting in overall cooling (-0.26±0.14 K). However, the spatial pattern of the temperature response shows substantial differences from that of the forcing. This can be clearly seen over the Arctic and large part of the oceans, which feature pronounced cooling despite the regional positive ERF. The temperature response to ozone reflects relatively more tightly the spatial pattern of ERF: warming (cooling) from positive (negative) forcing in association with tropospheric ozone increase (stratospheric ozone depletion). However, ozone-related zonal mean temperature responses are generally small in magnitude and indistinguishable from zero except over the polar regions (Figure 4). For stratospheric ozone depletion, despite the relatively small global mean ERF and temperature response, it has significant impacts on Southern Hemisphere climate by modulating large-scale circulation (Thompson et al., 2011; Previdi and Polvani, 2014; Dennison et al., 2015; Wu and Polvani, 2017). The Antarctic cooling in response to stratospheric ozone depletion is larger than those reported by recent works (McLandress et al., 2011; England et al., 2016; Chiodo et al., 2017; Karpechko et al., 2018). This may imply that the Antarctic temperature response to stratospheric ozone depletion can be even greater than currently estimated once the climate has fully equilibrated.

The above analysis indicates that the pattern of surface air temperature response does not necessarily follow the forcing, particularly in the case of aerosols and stratospheric ozone depletion. To point this out even more clearly, we investigate the sensitivity of the temperature response per unit ERF globally as well as regionally. Figure 6 shows the ERF sensitivity for various forcing agents. When regional mean temperature changes are normalized by global mean ERFs, the sensitivity values, over all regions, are greater in the

experiment where all forcings take effects simultaneously compared to the experiment where GHGs take effect alone. This also applies when regional mean temperature responses are normalized by regional mean ERFs, with exceptions over the Arctic (Figure 6d), Europe (Figure 6g) and North America (Figure 6i). The sensitivity is largest over the Arctic (Figure 6d), due to large local sea-ice albedo-related positive feedbacks. Anthropogenic aerosols, surprisingly, result in a much larger sensitivity when normalised against global mean ERF, particularly over the Arctic, North America and Asia (Figure 6k). The sensitivity to regional mean aerosol ERF is negative over the Arctic, the Southern Ocean (Figure 6f), Europe (Figure 6g) and the USA (Figure 6i). This, as clearly shown in Figure 4b and 4f, indicates that forcing and temperature response can be of opposite sign for aerosols over those regions. For tropospheric ozone, the sensitivity displays large variations across regions. Note the large and negative sensitivity (<-80 K m^2 W^{-1}) over South America. This is explainable given the increase in temperature (Figure 4g), despite the statistically insignificant and negative forcing (Figure 4c). Finally, stratospheric ozone has the smallest sensitivity at global scale and large variability and uncertainties from region to region.

The negative relationship between aerosol ERF and temperature response warrants further discussion. Of particular interest is the large negative sensitivity value over the Arctic. Further analysis (Figure S3) shows that the pronounced Arctic cooling is associated with reduced surface net radiation and cloud fraction, an overall extension of the sea ice-covered areas, and a widespread low-tropospheric anomalous anticyclone. Interestingly, the high-latitude hemispheric-wide anomalies (e.g., temperature, sea ice extent, sea level pressure) are dominated by prominent changes in the North Atlantic and Barents Sea sector. Here, the low-level flow, part of an extensive cyclonic circulation centred over Central Europe (Figure S3a) developing in response to the large regional aerosol reduction and subsequent local warming (Figure 4f), is anomalously southward and counteracts the climatological southwesterlies.

(Figure S3a) This reduced the northward transport of moisture to the Arctic region, suppressing cloud formation (Morrison et al., 2019). As clouds reduce (Figure S3b), the increase in surface downward shortwave radiation is overwhelmed by a much larger increase in the surface net longwave component, resulting in reductions in net radiation at the surface (Figure S3c). As a result, the Arctic surface cools and sea ice expands, leading to anomalous Arctic high pressure (Figure S3a) and increases in surface albedo (Figure S3d). This further enhances the cooling through the sea-ice-albedo feedbacks. Therefore, more cold air is transported southward partially opposing the warming associated with the positive ERF. The above analysis indicates the importance of atmospheric circulation adjustments, rather than the local forcing, in influencing the surface temperature changes at high latitudes (Undorf et al., 2018).

3.3 Precipitation response

The precipitation response patterns are shown in Figure 7 (see also Figure S4 for the zonal mean changes). GHG increases enhance global mean precipitation by 0.06±0.02 mm day^{-1}, with the largest amounts in the eastern equatorial Pacific and the extratropical regions of both hemispheres. Changes in aerosols lead to a global mean precipitation reduction (-0.04±0.02mm day^{-1}), with most pronounced changes over Asia (-0.13±0.07 mm day^{-1}) and the Western Pacific (Figure 7b). Also, a small but noticeable precipitation increase (+0.03±0.05 mm day^{-1}) is found over Europe associated with regional aerosol reductions. The zonal mean precipitation change features a decrease at almost all latitudes, and particularly over the tropics. The precipitation responses (both the spatial pattern and zonal mean changes) to GHGs and aerosols closely resemble those associated with the $2\times CO_2$ and $5\times SO_4$ experiments, respectively, of the Precipitation Driver and Response Model Inter-comparison Project (PDRMIP; Samset et al. (2016)).

The precipitation response to tropospheric ozone increase (Figure 7c) bears resemblance to that associated with aerosol changes, particularly over Asia, Southeast Asia and the Pacific Ocean. However, changes in the zonal mean profile show an enhancement of precipitation at the equator, along with a global mean increase of +0.01 mm day^{-1}. Precipitation changes due to stratospheric ozone depletion (Figure 7d) are broadly opposite to those associated with tropospheric ozone increase. More specifically, the precipitation increases over the Western Pacific but decreases over the Eastern Pacific and the Indian Ocean, resulting in an overall weak northward shift of the ITCZ. This generally agrees with Brönnimann et al. (2017) who reported that stratospheric ozone depletion has led precipitation to increase at the northern flank of the South Pacific Convergence Zone and to decrease at the south.

The global apparent hydrological sensitivity in equilibrium is estimated to be 1.4 % K^{-1} in the all forcing experiment, while the estimate from the LENS transient response is 1.3 % K^{-1}. These estimates fit well within the range (1-3 % K^{-1}) reported by phase 5 of the Coupled Model Intercomparison Project (CMIP5; Fläschner et al. (2016)), and suggest that the global apparent hydrological sensitivity does not differ sensibly between equilibrium and transient climate responses in CESM1. However, it worth pointing out that, compared to the all forcing experiment, the sensitivity is larger in magnitude when calculated for individual forcing including GHGs (1.8 % K^{-1}), aerosols (4.5 % K^{-1}) and tropospheric ozone (2.3 % K^{-1}).

To gain further insight into the characteristics of the precipitation responses, we examined changes in the daily precipitation distributions by analysing variations in the frequency distributions (Figure 8). Whilst precipitation is, by nature, spatially heterogeneous which may result, when averaged over large regions, into a partial cancellation between opposite sign anomalies over different sub-regions and thus to a smaller signal, we believe that large-scale averages provide useful information to identify large-scale patterns of

changes which are directly linked to the management of country-wide resources and to the development of adaptation strategies. To facilitate quantitative discussion, we define three precipitation categories: light (precipitation $\leq 10^{th}$ percentile of the 1970 climatological distribution), moderate (10^{th}-90^{th} percentile) and heavy-to-extreme ($\geq 90^{th}$ percentile) precipitation. Note carefully these definitions are only for the purpose of quantitative analysis. Figure 8 shows the global (Figure 8a) and global land-only (Figure 8b) precipitation distributions; the remaining panels compare Asia (Figure 8c) to Europe (Figure 8d). These two regions have opposite 1970-2010 aerosol changes, albeit of different magnitude (Figure 2), allowing us to examine whether the corresponding precipitation distributions also display opposite responses.

In response to the 1970-2010 changes in all forcings, the global mean daily precipitation distribution shifts to higher values, resulting in a mean shift of the precipitation distribution by +0.06 mm day^{-1} (+1.8%). This is primarily associated with GHG increases (+1.9%). The impact of tropospheric ozone increase on the distribution is similar but secondary (+0.31%) compared to GHGs. By comparison, anthropogenic aerosol increases and stratospheric ozone depletion shift the distribution towards lower values, resulting in a mean precipitation change of -1.1% and -0.03%, respectively. Land-only precipitation changes resemble those at global scale (land + ocean), but feature a relatively stronger effect of ozone changes together with a smaller effect of GHGs.

Examining now regional responses, the all forcings-driven changes result in a flatter and wider distribution of daily precipitation over Asia (Figure 8c). This is primarily associated with aerosol increases (-4.2%, -0.13 mm day^{-1}) which outweigh the effects of GHGs (+3.4%, +0.10 mm day^{-1}) and tropospheric ozone (+0.1%, +0.00 mm day^{-1}) increase. Noticeably, aerosol increases result in an increase of light (+1.0%) and moderate (+1.3%) precipitation, concurrently with a suppression of heavy-to-extreme precipitation (-2.3%). The

magnitude of these changes is larger than that associated with all forcings (0.5%, -0.3% and -0.2%, respectively). Over Europe (Figure 8d), changes in the daily precipitation distribution are also strongly influenced by aerosols, but in the opposite way (+0.05 mm day^{-1}, +2.6%) to Asia: aerosol reduction leads the heavy-to-extreme precipitation in Europe to increase by 3.2%, accounting for 55% of the 1970-2010 total increase in heavy precipitation. Meanwhile, light and moderate precipitation are suppressed by -0.2% and -3.0%, respectively. Compared to aerosols, there is a relatively smaller contribution from GHG increases (a mean change of +0.03 mm day^{-1}, +1.3%), while the effects of tropospheric ozone increase are approximately balanced by those due to stratospheric ozone depletion.

In summary, changes in the precipitation distribution over Asia and Europe highlight the dominant role of aerosols over other forcings in modulating local precipitation. This is particularly important for heavy-to-extreme precipitation, being reduced from 10% to 7.7% by aerosol increases over Asia, and increased from 10% to 13.2% by aerosol decreases over Europe. The contrast between Asia and Europe, therefore, demonstrates the effectiveness of increased (decreased) aerosols in weakening (enhancing) precipitation, respectively.

4 Discussion and conclusions

Human activities have altered both composition and (chemical and physical) properties of the atmosphere since the industrial era (Acosta Navarro et al., 2017). Such changes are even more distinctive during the past four decades (1970-2010). Specifically, on top of the steady GHG increases, there are contrasting trends of air pollutant emissions between developing and developed regions (Hoesly et al., 2018; Wang et al., 2018b; Zheng et al., 2018; Aas et al., 2019), as well as opposite trends between tropospheric and stratospheric ozone changes (Checa-Garcia et al., 2018). Employing CESM1, we carried out time-slice simulations to investigate the effective radiative forcing and climate responses to 1970-2010

changes in these climate forcers, emphasizing the comparison between the individual impacts of GHGs and SLCFs.

Changes in atmospheric composition during 1970-2010 brought about a TOA total ERF of 1.56±0.45 W m^{-2}, mostly due to changes in GHGs (1.50±0.44 W m^{-2}) with secondary contributions from anthropogenic aerosols, tropospheric ozone increase and stratospheric ozone depletion (-0.11±0.14, 0.24 ± 0.01 and -0.07±0.15 W m^{-2}, respectively). These estimates are consistent with the ones reported by the AR5 for the period 1970-2010 (GHGs: 1.48 W m^{-2}; aerosols: -0.20 W m^{-2}; tropospheric ozone increase: 0.14 W m^{-2}, and stratospheric ozone depletion: 0.04 W m^{-2}, see Table AII.12, Chapter 8.1 in Stocker et al. (2013)). Our estimate for tropospheric ozone increase is larger than the AR5 one. This is consistent with Myhre et al. (2017a) who found that ozone forcing is larger than the AR5 estimate during the period 1990-2015, likely due to an increase in NO_x emissions which is twice larger than the emission data used in AR5. The IPCC AR4 (Figure SPM.5) multi-model experiments reported that, in the case where all forcing agents are fixed at their 2000 levels, there is ~0.4 K of additional warming by 2100 due to the slow response of the ocean. The additional warming is around 1/3 of the 1900-2000 transient warming, and 2/3 of the amount occurred in the period 1970-2000 (Meehl et al., 2007). We show that compared to the transient changes, there is an additional global warming (~0.6 K) and precipitation increase (~0.03 mm day^{-1}) when present-day climate equilibrates to 1970-2010 emission changes. This in general is consistent with AR4, while the differences can be explained by differences in experimental design. The committed warming may result in changes in many other aspects of the climate system (Schlesinger, 1986; Tricot and Berger, 1987; Williams et al., 2016; Yoshimori et al., 2016) and associated impacts such as global scale precipitation changes discussed above.

The equilibrium climate responses to GHGs and aerosols, in general, agree with literature showing that the historical global mean temperature and precipitation changes are dominated by GHGs (Taylor and Penner, 1994; Min et al., 2011; Stocker et al., 2013; Wang et al., 2016), while aerosols play important roles in regional precipitation changes (e.g., the drying trend of the Asian monsoon (Yihui and Chan, 2005; Lau and Kim, 2006; Bollasina et al., 2011; Ganguly et al., 2012; Polson et al., 2014; Song et al., 2014; Lau and Kim, 2017; Ma et al., 2017)). However, as opposed to those arguing that the spatial patterns of the climate responses to GHGs and aerosols are similar (Xie et al., 2013; Kasoar et al., 2018; Persad et al., 2018), our results demonstrate that the climate forcing and responses to SLCFs are with large spatial heterogeneity and uncertainty (Shindell et al., 2015; Aamaas et al., 2017). Xie et al. (2016) estimated a global mean ERF of +0.46 W m^{-2}, a temperature increase of +0.36 K and precipitation increase of +0.02 mm day^{-1} due to 1850-2013 tropospheric ozone increase. These estimates all agree in sign with our estimates for the period 1970-2010, and are around 2-3 times larger in magnitudes. Also, note that the spatial patterns of the precipitation response to tropospheric ozone increase show good agreement with each other (compare Figure 7c with Figure 5c of Xie et al. (2016)). For stratospheric ozone depletion, we acknowledge that the annual global mean values reported here may not be able to reflect fully the impacts which are mainly through modulating austral summer atmospheric (subpolar to tropical latitudes) circulations (McLandress et al., 2011; England et al., 2016; Chiodo et al., 2017; Karpechko et al., 2018). This will be explicitly investigated in our future works.

Effective radiative forcing is generally deemed to be a useful indicator of temperature changes (Shindell and Faluvegi, 2009; Myhre et al., 2013; Shindell et al., 2015; Forster et al., 2016; Lewinschal et al., 2019). However, it has also been pointed out that forcing and temperature response are not necessarily collocated, due to many other climate processes and feedbacks such as the atmospheric and oceanic heat transport, and atmospheric circulation

adjustments (Boer and Yu, 2003; Shindell et al., 2010; Bellouin et al., 2016; Persad and Caldeira, 2018). Nevertheless, possible links between forcing and temperature response, at least at large scale such as within latitudinal bands, has been suggested (Shindell and Faluvegi, 2009; Flanner, 2013; Shindell, 2014; Shindell et al., 2015). The major appeal behind this is that such links may help develop simplified metrics for quickly evaluating the climate impacts of possible mitigation strategies in the future (Aamaas et al., 2017; Lewinschal et al., 2019). The links between forcing and temperature response found by above works, with large uncertainties and dependency upon many factors, are derived from highly idealized model experiments which represent only a few facets of the actual climate. In addition, as pointed out by Lewinschal et al. (2019), the temperature response sensitivity also depends on the magnitude of emissions. This suggests that the conclusions (sensitivity values) can vary substantially upon experimental designs with emissions of different magnitude and source location (Feichter et al., 2004; Ming and Ramaswamy, 2009; Wilcox et al., 2015). We show here that the relationship between forcing and temperature response may work for GHGs, but not for SLCFs; the relationship shows considerable variability depending on the region and forcing agent. Our results agree with recent works showing that the regional pattern of climate responses to SLCFs depend on the specific forcing agent, as well as timing and location of emissions (Aamaas et al., 2017; Persad and Caldeira, 2018; Lewinschal et al., 2019). However, the caveat is that the results/conclusions presented here may be model dependent. This is particularly the case for SLCFs, and aerosols in particular, whose climate forcing and response are highly heterogeneous and are not well constrained in present generation climate models.

Additionally, we found that

- Once the present-day climate has reached equilibrium, both the global mean temperature and precipitation changes would be twice as much as those in the transient 1970-2010 simulations.
- Increases in GHGs and tropospheric ozone enhance global mean precipitation and shift the daily precipitation distribution to larger amounts. On the contrary, the overall aerosol increases and stratospheric ozone depletion suppress global mean precipitation and shift the daily distribution toward smaller amounts.
- Compared to the global scale, the effectiveness of SLCFs in changing the characteristics of the daily precipitation distribution is stronger over regional scales. This is especially important for regions such as Asia and Europe where precipitation changes, and the frequency of heavy-to-extreme precipitation in particular, are dominated by changes in aerosols rather than GHGs.

In summary, we show that the present-day climate response to the recent (1970-2010) emission changes is far from being in equilibrium, implying that even with current emission levels we have observed only a fraction of the equilibrium changes to climate and associated risks (Mauritsen and Pincus, 2017). In addition, the concept of effective radiative forcing should be used very cautiously to interpret the impacts of SLCFs. A very representative example is aerosols that are shown to outweigh GHGs in regional precipitation changes, and modulate heavy to extreme precipitation significantly. Given the possibility that emissions/concentrations of SLCFs will decline in the coming decades, it is crucial to reduce the uncertainties in our understanding of the climate impacts of SLCFs. This is critically important to achieve more robust near-future climate projections and to manage climate risks (e.g., drought, flood, heatwaves, air pollution and etc.) more effectively.

Acknowledgement

A. Zhao was jointly funded by the University of Edinburgh and the China Scholarships. D. S. Stevenson acknowledges support from NERC grant NE/S009019/1 and NE/N003411/1. M. A. Bollasina was supported by the UK-China Research and Innovation Partnership Fund through the Met Office Climate Science for Service Partnership (CSSP) China as part of the Newton Fund. This work made use of computation resources on the UK ARCHER National Supercomputing Service (http://www.archer.ac.uk). The authors thank the Community Earth System Model project at NCAR. We are grateful to Gary Strand (NCAR) for providing the model dumps and all his kind help. We thank the three anonymous reviewers for their very constructive and valuable comments. Special thanks go to the EDGAR team and Monica Crippa in particular. The reanalysis and observational data sets used here are publicly available and properly cited. Other model outputs analysed here can be freely accessed through the Edinburgh DataShare (https://doi.org/10.7488/ds/2530).

References

Aamaas, B., T. K. Berntsen, J. S. Fuglestvedt, K. P. Shine, and W. J. Collins (2017), Regional temperature change potentials for short-lived climate forcers based on radiative forcing from multiple models, Atmospheric Chemistry and Physics, 17(17), 10795-10809.

Aas, W., A. Mortier, V. Bowersox, R. Cherian, G. Faluvegi, H. Fagerli, J. Hand, Z. Klimont, C. Galy-Lacaux, and C. M. Lehmann (2019), Global and regional trends of atmospheric sulfur, Scientific reports, 9(1), 953.

Acosta Navarro, J. C., A. M. Ekman, F. S. Pausata, A. Lewinschal, V. Varma, Ø. Seland, M. Gauss, T. Iversen, A. Kirkevåg, and I. Riipinen (2017), Future response of temperature and precipitation to reduced aerosol emissions as compared with increased greenhouse gas concentrations, Journal of Climate, 30(3), 939-954.

Allen, R. J., and S. C. Sherwood (2011), The impact of natural versus anthropogenic aerosols on atmospheric circulation in the Community Atmosphere Model, Climate dynamics, 36(9-10), 1959-1978.

Andreae, M., and D. Rosenfeld (2008), Aerosol–cloud–precipitation interactions. Part 1. The nature and sources of cloud-active aerosols, Earth-Science Reviews, 89(1), 13-41.

Bellouin, N., L. Baker, Ø. Hodnebrog, D. Olivie, R. Cherian, C. Macintosh, B. Samset, A. Esteve, B. Aamaas, and J. Quaas (2016), Regional and seasonal radiative forcing by perturbations to aerosol and ozone precursor emissions, Atmospheric Chemistry and Physics, 16(21), 13885-13910.

Boer, G., and B. Yu (2003), Climate sensitivity and response, Climate Dynamics, 20(4), 415-429.

Bollasina, M. A., Y. Ming, and V. Ramaswamy (2011), Anthropogenic aerosols and the weakening of the South Asian summer monsoon, science, 334(6055), 502-505.

Boucher, O., D. Randall, P. Artaxo, C. Bretherton, G. Feingold, P. Forster, V.-M. Kerminen, Y. Kondo, H. Liao, and U. Lohmann (2013), Clouds and aerosols, in Climate change 2013: the physical science basis. Contribution of Working Group I to the Fifth Assessment Report of the Intergovernmental Panel on Climate Change, edited, pp. 571-657, Cambridge University Press.

Brönnimann, S., M. Jacques-Coper, E. Rozanov, A. M. Fischer, O. Morgenstern, G. Zeng, H. Akiyoshi, and Y. Yamashita (2017), Tropical circulation and precipitation response to ozone depletion and recovery, Environmental Research Letters, 12(6), 064011.

Caldwell, P. M., M. D. Zelinka, and S. A. Klein (2018), Evaluating Emergent Constraints on Equilibrium Climate Sensitivity, Journal of Climate, 31(10), 3921-3942.
Checa-Garcia, R., M. I. Hegglin, D. Kinnison, D. A. Plummer, and K. P. Shine (2018), Historical tropospheric and stratospheric ozone radiative forcing using the CMIP6 database, Geophysical Research Letters, 45(7), 3264-3273.
Chen, W., and B. Dong (2018), Anthropogenic impacts on recent decadal change in temperature extremes over China: relative roles of greenhouse gases and anthropogenic aerosols, Climate Dynamics, 1-18.
Chiodo, G., L. Polvani, and M. Previdi (2017), Large increase in incident shortwave radiation due to the ozone hole offset by high climatological albedo over Antarctica, Journal of Climate, 30(13), 4883-4890.
Conley, A. J., R. Garcia, D. Kinnison, J.-F. Lamarque, D. Marsh, M. Mills, A. K. Smith, S. Tilmes, F. Vitt, and H. Morrison (2012), Description of the NCAR community atmosphere model (CAM 5.0), NCAR technical note.
Crippa, M., G. Janssens-Maenhout, F. Dentener, D. Guizzardi, K. Sindelarova, M. Muntean, R. Van Dingenen, and C. Granier (2016), Forty years of improvements in European air quality: regional policy-industry interactions with global impacts, Atmospheric Chemistry and Physics, 16(6), 3825-3841.
Dallafior, T., D. Folini, R. Knutti, and M. Wild (2016), Mixed-layer ocean responses to anthropogenic aerosol dimming from 1870 to 2000, Journal of Geophysical Research: Atmospheres, 121(1), 49-66.
Dennison, F. W., A. J. McDonald, and O. Morgenstern (2015), The effect of ozone depletion on the Southern Annular Mode and stratosphere-troposphere coupling, Journal of Geophysical Research: Atmospheres, 120(13), 6305-6312.
England, M. R., L. M. Polvani, K. L. Smith, L. Landrum, and M. M. Holland (2016), Robust response of the Amundsen Sea Low to stratospheric ozone depletion, Geophysical Research Letters, 43(15), 8207-8213.
Fan, J., Y. Wang, D. Rosenfeld, and X. Liu (2016), Review of aerosol–cloud interactions: Mechanisms, significance, and challenges, Journal of the Atmospheric Sciences, 73(11), 4221-4252.
Feichter, J., E. Roeckner, U. Lohmann, and B. Liepert (2004), Nonlinear aspects of the climate response to greenhouse gas and aerosol forcing, Journal of climate, 17(12), 2384-2398.
Figueres, C., C. Le Quéré, A. Mahindra, O. Bäte, G. Whiteman, G. Peters, and D. Guan (2018), Emissions are still rising: ramp up the cuts, edited, Nature Publishing Group.
Flanner, M. G. (2013), Arctic climate sensitivity to local black carbon, Journal of Geophysical Research: Atmospheres, 118(4), 1840-1851.
Fläschner, D., T. Mauritsen, and B. Stevens (2016), Understanding the intermodel spread in global-mean hydrological sensitivity, Journal of Climate, 29(2), 801-817.
Forster, P. M., T. Richardson, A. C. Maycock, C. J. Smith, B. H. Samset, G. Myhre, T. Andrews, R. Pincus, and M. Schulz (2016), Recommendations for diagnosing effective radiative forcing from climate models for CMIP6, Journal of Geophysical Research: Atmospheres, 121(20).
Ganguly, D., P. J. Rasch, H. Wang, and J. h. Yoon (2012), Fast and slow responses of the South Asian monsoon system to anthropogenic aerosols, Geophysical Research Letters, 39(18).
Hodnebrog, Ø., G. Myhre, P. M. Forster, J. Sillmann, and B. H. Samset (2016), Local biomass burning is a dominant cause of the observed precipitation reduction in southern Africa, Nature communications, 7, 11236.

Hoesly, R. M., S. J. Smith, L. Feng, Z. Klimont, G. Janssens-Maenhout, T. Pitkanen, J. J. Seibert, L. Vu, R. J. Andres, and R. M. Bolt (2018), Historical (1750–2014) anthropogenic emissions of reactive gases and aerosols from the Community Emissions Data System (CEDS), Geoscientific Model Development, 11(1), 369-408.
Hossaini, R., M. P. Chipperfield, S. A. Montzka, A. A. Leeson, S. S. Dhomse, and J. A. Pyle (2017), The increasing threat to stratospheric ozone from dichloromethane, Nature communications, 8, 15962.
Hsu, J., and M. J. Prather (2009), Stratospheric variability and tropospheric ozone, Journal of Geophysical Research: Atmospheres, 114(D6).
Huffman, G. J., R. F. Adler, P. Arkin, A. Chang, R. Ferraro, A. Gruber, J. Janowiak, A. McNab, B. Rudolf, and U. Schneider (1997), The global precipitation climatology project (GPCP) combined precipitation dataset, Bulletin of the American Meteorological Society, 78(1), 5-20.
Hurrell, J. W., M. M. Holland, P. R. Gent, S. Ghan, J. E. Kay, P. J. Kushner, J.-F. Lamarque, W. G. Large, D. Lawrence, and K. Lindsay (2013), The community earth system model: a framework for collaborative research, Bulletin of the American Meteorological Society, 94(9), 1339-1360.
Hwang, Y. T., D. M. Frierson, and S. M. Kang (2013), Anthropogenic sulfate aerosol and the southward shift of tropical precipitation in the late 20th century, Geophysical Research Letters, 40(11), 2845-2850.
Jong, B.-T., M. Ting, R. Seager, N. Henderson, and D. E. Lee (2018), Role of equatorial Pacific SST forecast error in the late winter California precipitation forecast for the 2015/16 El Niño, Journal of Climate, 31(2), 839-852.
Kalnay, E., M. Kanamitsu, R. Kistler, W. Collins, D. Deaven, L. Gandin, M. Iredell, S. Saha, G. White, and J. Woollen (1996), The NCEP/NCAR 40-year reanalysis project, Bulletin of the American meteorological Society, 77(3), 437-471.
Karpechko, A. Y., A. C. Maycock, M. Abalos, H. Akiyoshi, J. M. Arblaster, C. I. Garfinkel, K. H. Rosenlof, and M. Sigmond (2018), Stratospheric Ozone Changes and Climate, Chapter 5 in Scientific Assessment of Ozone Depletion: 2018, Global Ozone Research and Monitoring Project–Report, 58.
Kasoar, M., D. Shawki, and A. Voulgarakis (2018), Similar spatial patterns of global climate response to aerosols from different regions, npj Climate and Atmospheric Science, 1(1), 12.
Kay, J., C. Deser, A. Phillips, A. Mai, C. Hannay, G. Strand, J. Arblaster, S. Bates, G. Danabasoglu, and J. Edwards (2015), The Community Earth System Model (CESM) large ensemble project: A community resource for studying climate change in the presence of internal climate variability, Bulletin of the American Meteorological Society, 96(8), 1333-1349.
Kuttippurath, J., and P. J. Nair (2017), The signs of Antarctic ozone hole recovery, Scientific reports, 7(1), 585.
Lamarque, J.-F., G. P. Kyle, M. Meinshausen, K. Riahi, S. J. Smith, D. P. van Vuuren, A. J. Conley, and F. Vitt (2011), Global and regional evolution of short-lived radiatively-active gases and aerosols in the Representative Concentration Pathways, Climatic change, 109(1-2), 191-212.
Lamarque, J.-F., T. C. Bond, V. Eyring, C. Granier, A. Heil, Z. Klimont, D. Lee, C. Liousse, A. Mieville, and B. Owen (2010), Historical (1850–2000) gridded anthropogenic and biomass burning emissions of reactive gases and aerosols: methodology and application, Atmospheric Chemistry and Physics, 10(15), 7017-7039.
Lau, K. M., and K. M. Kim (2006), Observational relationships between aerosol and Asian monsoon rainfall, and circulation, Geophysical Research Letters, 33(21).

Lau, W. K.-M., and K.-M. Kim (2017), Competing influences of greenhouse warming and aerosols on Asian summer monsoon circulation and rainfall, Asia-Pacific Journal of Atmospheric Sciences, 53(2), 181-194.
Lewinschal, A., A. M. Ekman, H.-C. Hansson, M. Sand, T. K. Berntsen, and J. Langner (2019), Local and remote temperature response of regional SO 2 emissions, Atmospheric Chemistry and Physics, 19(4), 2385-2403.
Li, C. McLinden, V. Fioletov, N. Krotkov, S. Carn, J. Joiner, D. Streets, H. He, X. Ren, and Z. Li (2017), India is overtaking China as the world's largest emitter of anthropogenic sulfur dioxide, Scientific reports, 7(1), 14304.
Liu, J., B. Wang, M. A. Cane, S.-Y. Yim, and J.-Y. Lee (2013), Divergent global precipitation changes induced by natural versus anthropogenic forcing, Nature, 493(7434), 656.
Liu, X., P.-L. Ma, H. Wang, S. Tilmes, B. Singh, R. Easter, S. Ghan, and P. Rasch (2015), Description and evaluation of a new 4-mode version of Modal Aerosol Module (MAM4) within version 5.3 of the Community Atmosphere Model, Geoscientific Model Development Discussions, 8(9).
Liu, X., R. C. Easter, S. J. Ghan, R. Zaveri, P. Rasch, X. Shi, J.-F. Lamarque, A. Gettelman, H. Morrison, and F. Vitt (2012), Toward a minimal representation of aerosols in climate models: Description and evaluation in the Community Atmosphere Model CAM5, Geoscientific Model Development, 5(3), 709.
Ma, S., T. Zhou, D. A. Stone, D. Polson, A. Dai, P. A. Stott, H. von Storch, Y. Qian, C. Burke, and P. Wu (2017), Detectable anthropogenic shift toward heavy precipitation over eastern China, Journal of Climate, 30(4), 1381-1396.
Marsh, D. R., M. J. Mills, D. E. Kinnison, J.-F. Lamarque, N. Calvo, and L. M. Polvani (2013), Climate change from 1850 to 2005 simulated in CESM1 (WACCM), Journal of climate, 26(19), 7372-7391.
Marvel, K., G. A. Schmidt, R. L. Miller, and L. S. Nazarenko (2016), Implications for climate sensitivity from the response to individual forcings, Nature Climate Change, 6(4), 386.
Mauritsen, T., and R. Pincus (2017), Committed warming inferred from observations, Nature Climate Change, 7(9), 652.
McLandress, C., T. G. Shepherd, J. F. Scinocca, D. A. Plummer, M. Sigmond, A. I. Jonsson, and M. C. Reader (2011), Separating the dynamical effects of climate change and ozone depletion. Part II: Southern Hemisphere troposphere, Journal of Climate, 24(6), 1850-1868.
Meehl, G. A., T. F. Stocker, W. D. Collins, P. Friedlingstein, T. Gaye, J. M. Gregory, A. Kitoh, R. Knutti, J. M. Murphy, and A. Noda (2007), Global climate projections.
Min, S.-K., X. Zhang, F. W. Zwiers, and G. C. Hegerl (2011), Human contribution to more-intense precipitation extremes, Nature, 470(7334), 378-381.
Ming, Y., and V. Ramaswamy (2009), Nonlinear climate and hydrological responses to aerosol effects, Journal of Climate, 22(6), 1329-1339.
Mitchell, J., S. Manabe, V. Meleshko, and T. Tokioka (1990), Equilibrium climate change and its implications for the future, Climate change: The IPCC scientific assessment, 131, 172.
Monks, P. S., A. Archibald, A. Colette, O. Cooper, M. Coyle, R. Derwent, D. Fowler, C. Granier, K. S. Law, and G. Mills (2015), Tropospheric ozone and its precursors from the urban to the global scale from air quality to short-lived climate forcer, Atmospheric Chemistry and Physics, 15(15), 8889-8973.
Morrison, A., J. Kay, W. Frey, H. Chepfer, and R. Guzman (2019), Cloud Response to Arctic Sea Ice Loss and Implications for Future Feedback in the CESM1 Climate Model, Journal of Geophysical Research: Atmospheres, 124(2), 1003-1020.

Myhre, W. Aas, R. Cherian, W. Collins, G. Faluvegi, M. Flanner, P. Forster, Ø. Hodnebrog, Z. Klimont, and M. T. Lund (2017a), Multi-model simulations of aerosol and ozone radiative forcing due to anthropogenic emission changes during the period 1990–2015, Atmospheric Chemistry and Physics, 17(4), 2709-2720.
Myhre, P. Forster, B. Samset, Ø. Hodnebrog, J. Sillmann, S. Aalbergsjø, T. Andrews, O. Boucher, G. Faluvegi, and D. Fläschner (2017b), PDRMIP: A precipitation driver and response model intercomparison project—Protocol and preliminary results, Bulletin of the American Meteorological Society, 98(6), 1185-1198.
Myhre, G., D. Shindell, F.-M. Bréon, W. Collins, J. Fuglestvedt, J. Huang, D. Koch, J.-F. Lamarque, D. Lee, and B. Mendoza (2013), Anthropogenic and natural radiative forcing, Climate change, 423.
Nychka, D., R. Buchberger, T. Wigley, B. Santer, K. Taylor, and R. Jones (2000), Confidence intervals for trend estimates with autocorrelated observations.
Ocko, I. B., V. Ramaswamy, and Y. Ming (2014), Contrasting climate responses to the scattering and absorbing features of anthropogenic aerosol forcings, Journal of Climate, 27(14), 5329-5345.
Olivier, J. G., J. A. Van Aardenne, F. J. Dentener, V. Pagliari, L. N. Ganzeveld, and J. A. Peters (2005), Recent trends in global greenhouse gas emissions: regional trends 1970–2000 and spatial distributionof key sources in 2000, Environmental Sciences, 2(2-3), 81-99.
Persad, G. G., and K. Caldeira (2018), Divergent global-scale temperature effects from identical aerosols emitted in different regions, Nature communications, 9(1), 3289.
Persad, G. G., Y. Ming, Z. Shen, and V. Ramaswamy (2018), Spatially similar surface energy flux perturbations due to greenhouse gases and aerosols, Nature communications, 9(1), 3247.
Polson, D., M. Bollasina, G. Hegerl, and L. Wilcox (2014), Decreased monsoon precipitation in the Northern Hemisphere due to anthropogenic aerosols, Geophysical Research Letters, 41(16), 6023-6029.
Previdi, M., and L. M. Polvani (2014), Climate system response to stratospheric ozone depletion and recovery, Quarterly Journal of the Royal Meteorological Society, 140(685), 2401-2419.
Riahi, K., A. Grübler, and N. Nakicenovic (2007), Scenarios of long-term socio-economic and environmental development under climate stabilization, Technological Forecasting and Social Change, 74(7), 887-935.
Ropelewski, C. F., and M. S. Halpert (1987), Global and regional scale precipitation patterns associated with the El Niño/Southern Oscillation, Monthly weather review, 115(8), 1606-1626.
Rugenstein, M., and J. Bloch-Johnson (2016), Equilibrium and Effective Climate Sensitivity, paper presented at AGU Fall Meeting Abstracts.
Samset, B., M. Sand, C. Smith, S. Bauer, P. Forster, J. Fuglestvedt, S. Osprey, and C. F. Schleussner Climate impacts from a removal of anthropogenic aerosol emissions, Geophysical Research Letters.
Samset, B., M. Sand, C. Smith, S. Bauer, P. Forster, J. Fuglestvedt, S. Osprey, and C. F. Schleussner (2018), Climate impacts from a removal of anthropogenic aerosol emissions, Geophysical Research Letters, 45(2), 1020-1029.
Samset, B., G. Myhre, P. Forster, Ø. Hodnebrog, T. Andrews, G. Faluvegi, D. Flaeschner, M. Kasoar, V. Kharin, and A. Kirkevåg (2016), Fast and slow precipitation responses to individual climate forcers: A PDRMIP multimodel study, Geophysical Research Letters, 43(6), 2782-2791.
Schlesinger, M. E. (1986), Equilibrium and transient climatic warming induced by increased atmospheric CO 2, Climate Dynamics, 1(1), 35-51.

Schmale, J., D. Shindell, E. von Schneidemesser, I. Chabay, and M. Lawrence (2014), Air pollution: clean up our skies, Nature News, 515(7527), 335.
Schmidt, G. A., D. T. Shindell, and K. Tsigaridis (2014), Reconciling warming trends, Nature Geoscience, 7(3), 158.
Shindell (2014), Inhomogeneous forcing and transient climate sensitivity, Nature Climate Change, 4(4), 274.
Shindell, G. Faluvegi, L. Rotstayn, and G. Milly (2015), Spatial patterns of radiative forcing and surface temperature response, Journal of Geophysical Research: Atmospheres, 120(11), 5385-5403.
Shindell, D., and G. Faluvegi (2009), Climate response to regional radiative forcing during the twentieth century, Nature Geoscience, 2(4), 294.
Shindell, D., M. Schulz, Y. Ming, T. Takemura, G. Faluvegi, and V. Ramaswamy (2010), Spatial scales of climate response to inhomogeneous radiative forcing, Journal of Geophysical Research: Atmospheres, 115(D19).
Smith, S. J., J. v. Aardenne, Z. Klimont, R. J. Andres, A. Volke, and S. Delgado Arias (2011), Anthropogenic sulfur dioxide emissions: 1850–2005, Atmospheric Chemistry and Physics, 11(3), 1101-1116.
Solomon, S. (1999), Stratospheric ozone depletion: A review of concepts and history, Reviews of Geophysics, 37(3), 275-316.
Solomon, S., D. J. Ivy, D. Kinnison, M. J. Mills, R. R. Neely, and A. Schmidt (2016), Emergence of healing in the Antarctic ozone layer, Science, 353(6296), 269-274.
Song, F., T. Zhou, and Y. Qian (2014), Responses of East Asian summer monsoon to natural and anthropogenic forcings in the 17 latest CMIP5 models, Geophysical Research Letters, 41(2), 596-603.
Stevenson, D., P. Young, V. Naik, J.-F. Lamarque, D. T. Shindell, A. Voulgarakis, R. B. Skeie, S. B. Dalsoren, G. Myhre, and T. K. Berntsen (2013), Tropospheric ozone changes, radiative forcing and attribution to emissions in the Atmospheric Chemistry and Climate Model Intercomparison Project (ACCMIP), Atmospheric Chemistry and Physics, 13(6), 3063-3085.
Stocker, D. Qin, G.-K. Plattner, M. Tignor, S. K. Allen, J. Boschung, A. Nauels, Y. Xia, V. Bex, and P. M. Midgley (2013), Climate change 2013: The physical science basis, Intergovernmental Panel on Climate Change, Working Group I Contribution to the IPCC Fifth Assessment Report (AR5)(Cambridge Univ Press, New York).
Stohl, A., B. Aamaas, M. Amann, L. H. Baker, N. Bellouin, T. K. Berntsen, O. Boucher, R. Cherian, W. Collins, and N. Daskalakis (2015), Evaluating the climate and air quality impacts of short-lived pollutants, Atmospheric Chemistry and Physics, 15(18), 10529-10566.
Taylor, K. E., and J. E. Penner (1994), Response of the climate system to atmospheric aerosols and greenhouse gases, Nature, 369(6483), 734.
Thompson, D. W., S. Solomon, P. J. Kushner, M. H. England, K. M. Grise, and D. J. Karoly (2011), Signatures of the Antarctic ozone hole in Southern Hemisphere surface climate change, Nature geoscience, 4(11), 741.
Tian, F., B. Dong, J. Robson, and R. Sutton (2018), Forced decadal changes in the East Asian summer monsoon: the roles of greenhouse gases and anthropogenic aerosols, Climate dynamics, 51(9-10), 3699-3715.
Tilmes, S., J.-F. Lamarque, L. Emmons, D. Kinnison, P. Ma, X. Liu, S. Ghan, C. Bardeen, S. Arnold, and M. Deeter (2015), Description and evaluation of tropospheric chemistry and aerosols in the Community Earth System Model (CESM1. 2), Geoscientific Model Development, 8, 1395-1426.
Tricot, C., and A. Berger (1987), Modelling the equilibrium and transient responses of global temperature to past and future trace gas concentrations, Climate Dynamics, 2(1), 39-61.

Undorf, S., M. Bollasina, B. Booth, and G. Hegerl (2018), Contrasting the Effects of the 1850–1975 Increase in Sulphate Aerosols from North America and Europe on the Atlantic in the CESM, Geophysical Research Letters, 45(21), 11,930-911,940.
Van Vuuren, D. P., J. Edmonds, M. Kainuma, K. Riahi, A. Thomson, K. Hibbard, G. C. Hurtt, T. Kram, V. Krey, and J.-F. Lamarque (2011), The representative concentration pathways: an overview, Climatic change, 109(1-2), 5.
Voigt, A., R. Pincus, B. Stevens, S. Bony, O. Boucher, N. Bellouin, A. Lewinschal, B. Medeiros, Z. Wang, and H. Zhang (2017), Fast and slow shifts of the zonal-mean intertropical convergence zone in response to an idealized anthropogenic aerosol, Journal of Advances in Modeling Earth Systems, 9(2), 870-892.
Wang, S.-P. Xie, and Q. Liu (2016), Comparison of climate response to anthropogenic aerosol versus greenhouse gas forcing: Distinct patterns, Journal of Climate, 29(14), 5175-5188.
Wang, L. Lin, M. Yang, Y. Xu, and J. Li (2017), Disentangling fast and slow responses of the East Asian summer monsoon to reflecting and absorbing aerosol forcings, Atmospheric Chemistry and Physics, 17(18), 11075-11088.
Wang, J. H. Jiang, H. Su, Y.-S. Choi, L. Huang, J. Guo, and Y. L. Yung (2018a), Elucidating the role of anthropogenic aerosols in Arctic sea ice variations, Journal of Climate, 31(1), 99-114.
Wang, P. Wang, N. Theys, D. Tong, F. Hendrick, Q. Zhang, and M. V. Roozendael (2018b), Spatial and temporal changes in SO 2 regimes over China in the recent decade and the driving mechanism, Atmospheric Chemistry and Physics, 18(24), 18063-18078.
Wilcox, L., E. Highwood, B. Booth, and K. Carslaw (2015), Quantifying sources of inter-model diversity in the cloud albedo effect, Geophysical Research Letters, 42(5), 1568-1575.
Williams, R. G., P. Goodwin, V. M. Roussenov, and L. Bopp (2016), A framework to understand the transient climate response to emissions, Environmental Research Letters, 11(1), 015003.
Wilmouth, D. M., R. J. Salawitch, and T. P. Canty (2017), Stratospheric Ozone Depletion and Recovery, in Green Chemistry, edited, pp. 177-209, Elsevier.
Wu, Y., and L. M. Polvani (2017), Recent trends in extreme precipitation and temperature over southeastern South America: The dominant role of stratospheric ozone depletion in the CESM Large Ensemble, Journal of Climate, 30(16), 6433-6441.
Xie, B., H. Zhang, Z. Wang, S. Zhao, and Q. Fu (2016), A modeling study of effective radiative forcing and climate response due to tropospheric ozone, Advances in Atmospheric Sciences, 33(7), 819-828.
Xie, S.-P., B. Lu, and B. Xiang (2013), Similar spatial patterns of climate responses to aerosol and greenhouse gas changes, Nature Geoscience, 6(10), 828-832.
Yang, H., and J. Zhu (2011), Equilibrium thermal response timescale of global oceans, Geophysical Research Letters, 38(14).
Yihui, D., and J. C. Chan (2005), The East Asian summer monsoon: an overview, Meteorology and Atmospheric Physics, 89(1-4), 117-142.
Yoshimori, M., M. Watanabe, H. Shiogama, A. Oka, A. Abe-Ouchi, R. Ohgaito, and Y. Kamae (2016), A review of progress towards understanding the transient global mean surface temperature response to radiative perturbation, Progress in Earth and Planetary Science, 3(1), 21.
Zhao, A., M. A. Bollasina, and D. S. Stevenson (2019), Strong influence of aerosol reductions on future heatwaves, Geophysical Research Letters, 46(9), 4913-4923.
Zhao, A. D., D. S. Stevenson, and M. A. Bollasina (2018), The role of anthropogenic aerosols in future precipitation extremes over the Asian Monsoon Region, Climate Dynamics, 1-22.

Zheng, B., D. Tong, M. Li, F. Liu, C. Hong, G. Geng, H. Li, X. Li, L. Peng, and J. Qi (2018), Trends in China's anthropogenic emissions since 2010 as the consequence of clean air actions, Atmospheric Chemistry and Physics, 18(19), 14095-14111.

Table 1 Overview of the equilibrium model experiments. They are, the baseline runs under 1970 (B70) and 2010 forcings (B10), fixing greenhouse gases and ozone in 1970 levels (SGO), fixing anthropogenic aerosol and their precursor gases in 1970 levels (SAA), fixing tropospheric and stratospheric ozone in 1970 levels (SOZ), and fixing tropospheric ozone in 1970 levels (STO). The climate responses are resolved into changes due to each forcing as follows: All=B10–B70; GHGs=SGO – SOZ; AAs= B10– SAA; Trop. O_3=B10–STO, Strat. O_3= STO–SOZ. The B70 simulation is initialised using the LENS transient simulation (ensemble member 34) at 1970, while all others are branched off from the LENS transient simulation (also member 34)) at 2010. All simulations are integrated into equilibrium (see the length (no. of years) of each simulation in brackets in the first column), and only the last 30 years of each run are used for analysis.

Simulation (length, years)	Initial condition	Greenhouse Gases (GHGs)	Anthropogenic aerosols (AAs)	Tropospheric ozone increase (Trop. O_3)	Stratospheric ozone depletion (Strat. O_3)
B70 (120)	1970	1970	1970	1970	1970
B10 (150)	2010	2010	2010	2010	2010
SAA (120)	2010	2010	1970	2010	2010
SGO (90)	2010	1970	2010	1970	1970
SOZ (150)	2010	2010	2010	1970	1970
STO (150)	2010	2010	2010	1970	2010

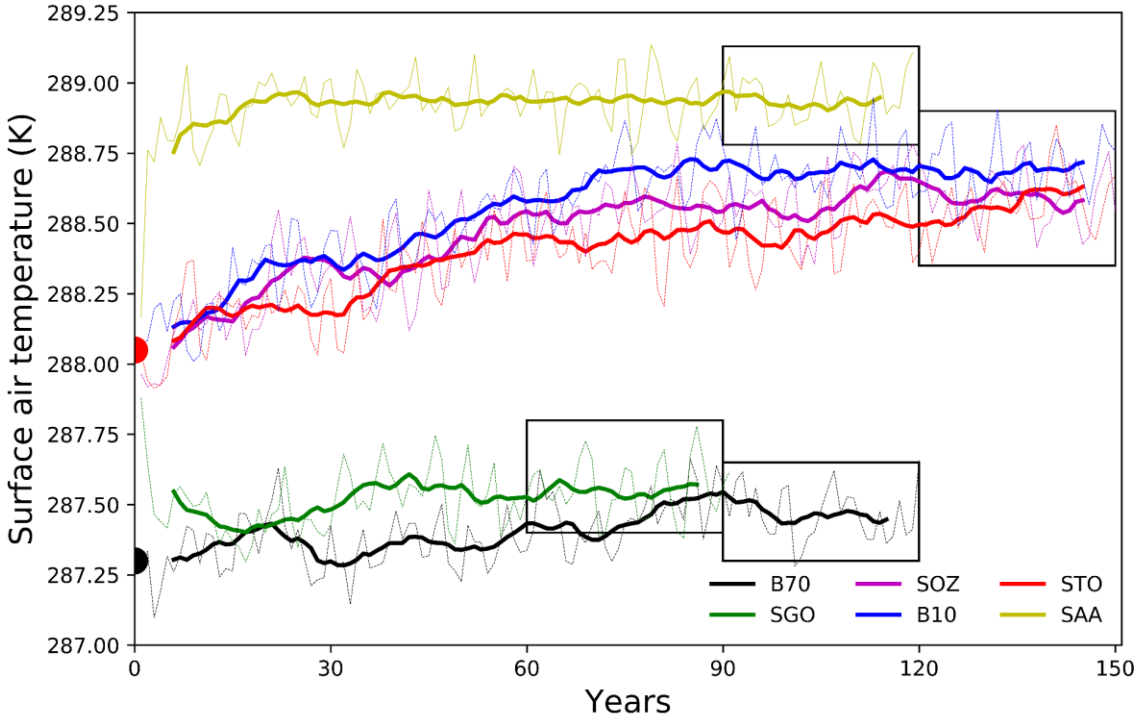

Figure 1 Time evolution (dashed lines and also the 11-years running mean in solid) of the global annual mean surface air temperature from the fully-coupled CESM1 baseline and perturbation runs. B70 and B10 refer to 1970 and 2010 all forcing runs, respectively. The perturbation simulations include SGO (fixing greenhouse gases plus ozone at their 1970 levels), SAA (fixing anthropogenic aerosols and their precursor gases at 1970 levels), SOZ (fixing ozone at 1970 levels) and STO (fixing tropospheric ozone at 1970 levels). The black boxes denote the last 30 years of each run analysed here. Note that all simulations except for B70 started from a same 2010 dump (red half-circle) while B70 stared from a 1970 dump (black half-circle), from the CESM1 large ensemble run (LENS, no 34). Also see Table 1 for the detailed experiment design.

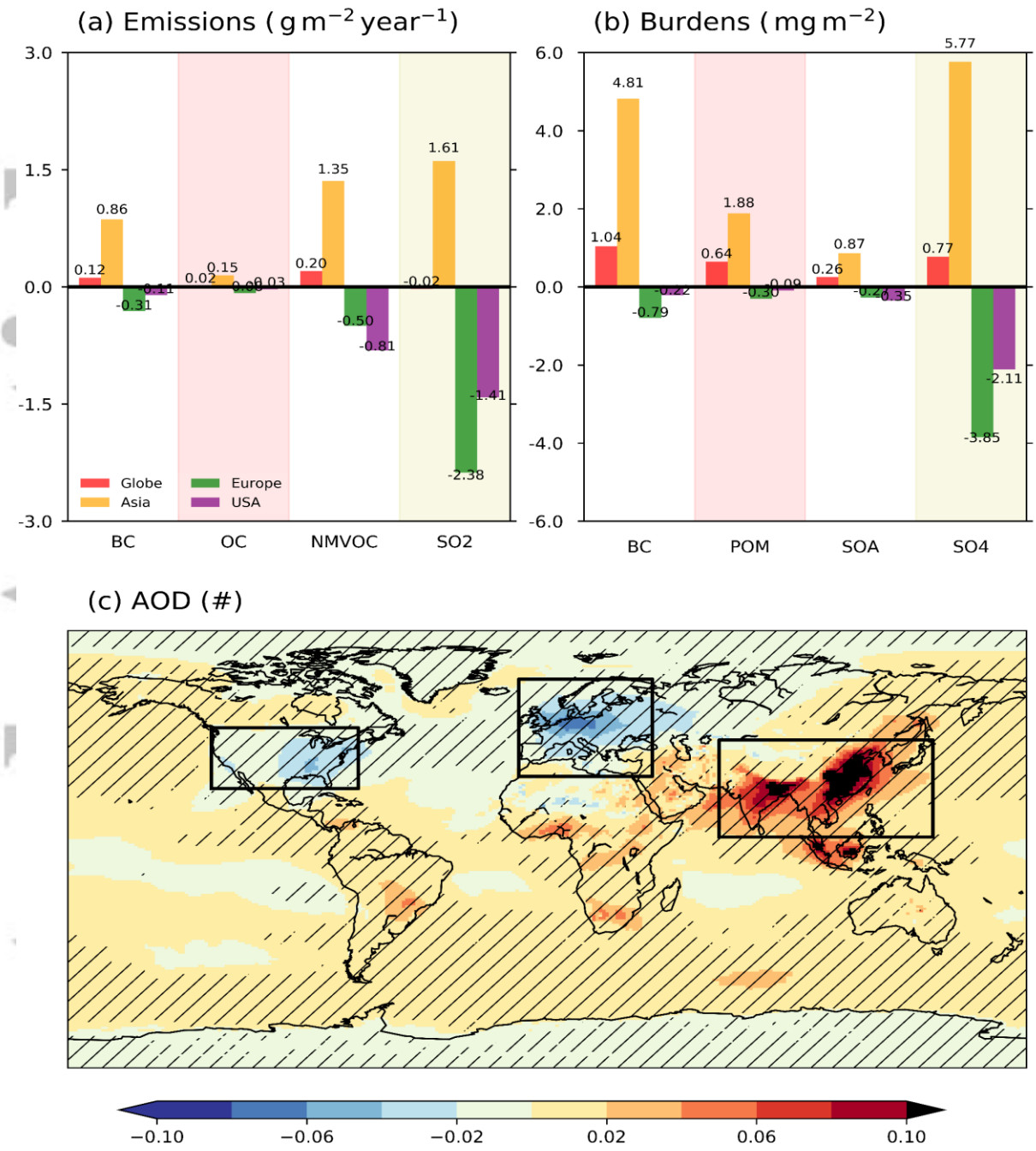

Figure 2 The 1970-2010 changes in (a) anthropogenic aerosol emissions (g m^{-2} $year^{-1}$), (b) CESM1 modelled aerosol burdens (mg m^{-2}) and (c) spatial distribution of aerosol optical depth (AOD) at a wavelength of 550nm. Emissions and burdens are shown as the area-weighted mean over the global scale (red), Asia (yellow), Europe (green) and USA (purple). The definitions of these regions are denoted by the black boxes in (c). Emissions include black carbon (BC), organic carbon (OC), non-methane volatile organic compounds (NMVOC) and sulphur dioxide (SO_2). Aerosol burdens include BC, primary organic carbon (POM), secondary organic carbon (SOA) and sulphate (SO_4). Hatches in (c), and also in all other figures, denote a statistically significant difference (5%), derived using a two-tailed student t-test. Note the emissions and burdens of BC are raised by a factor of 10 for legibility.

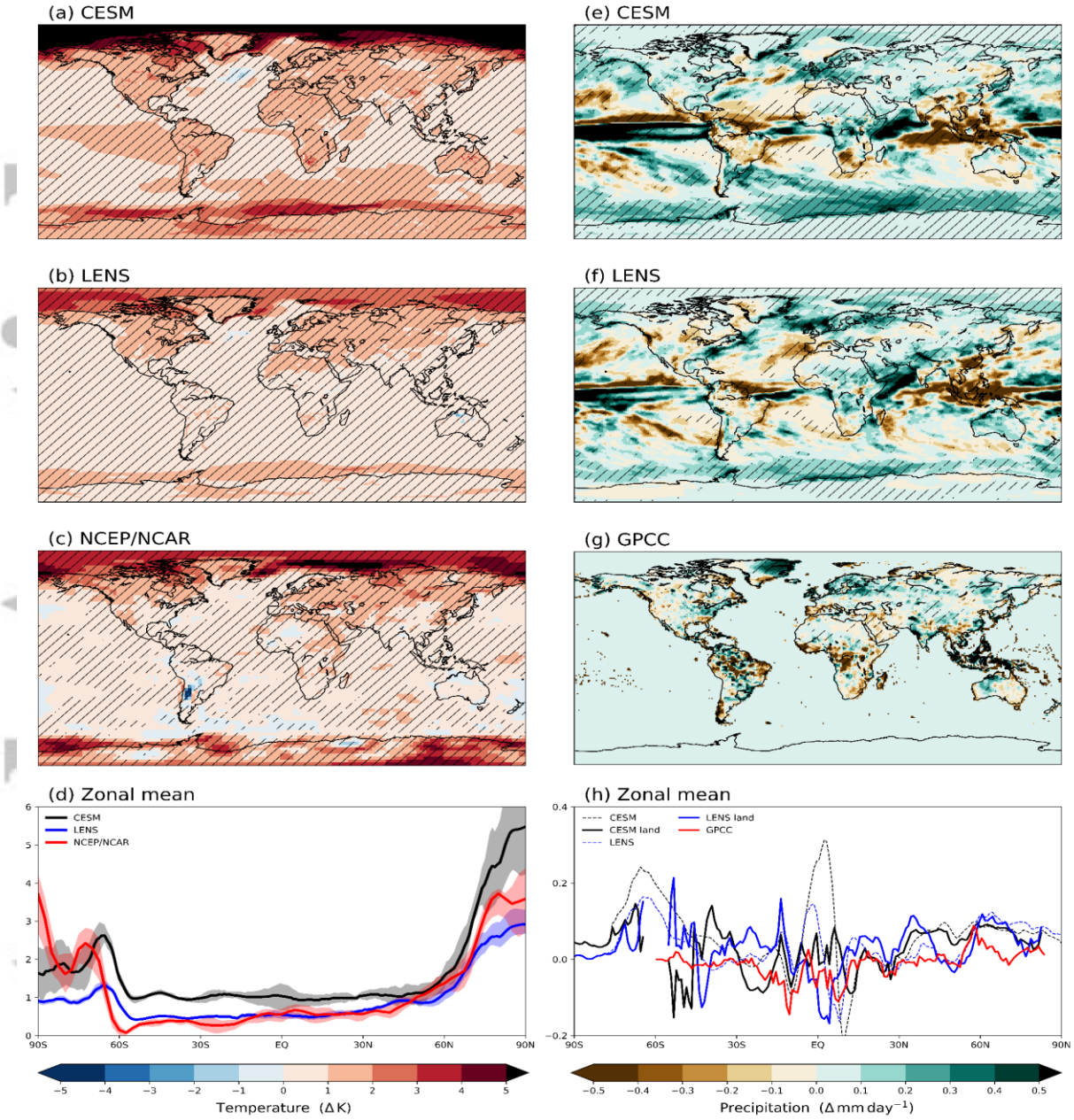

Figure 3 Comparisons of 1970-2010 changes in (a-d) annual mean surface air temperature and (e-h) precipitation. They are: (a, e) the difference between 1970 and 2010 equilibrium experiments in this study, (b, f) the difference between the time period 1963-1977 and 2003-2017 from the CESM1 large ensemble mean, (c, g) the difference between time period 1963-1977 and 2003-2017 from NCEP/NCAR surface temperature reanalysis and the Global Precipitation Climatology Centre (GPCC) precipitation, as well as (d, h) their zonal means (solid for mean changes, and shadings for the 2^{5th}-75^{th} uncertainty range). Solid curves in (h) are the corresponding land-only zonal mean precipitation changes, which are plotted to compare to the GPCC dataset that has data only over land. Hatches in the maps denote a statistically significant difference (5%), derived using a two-tailed student t-test. Note that to make the plot readable, the uncertainty range for zonal mean precipitation response is not shown.

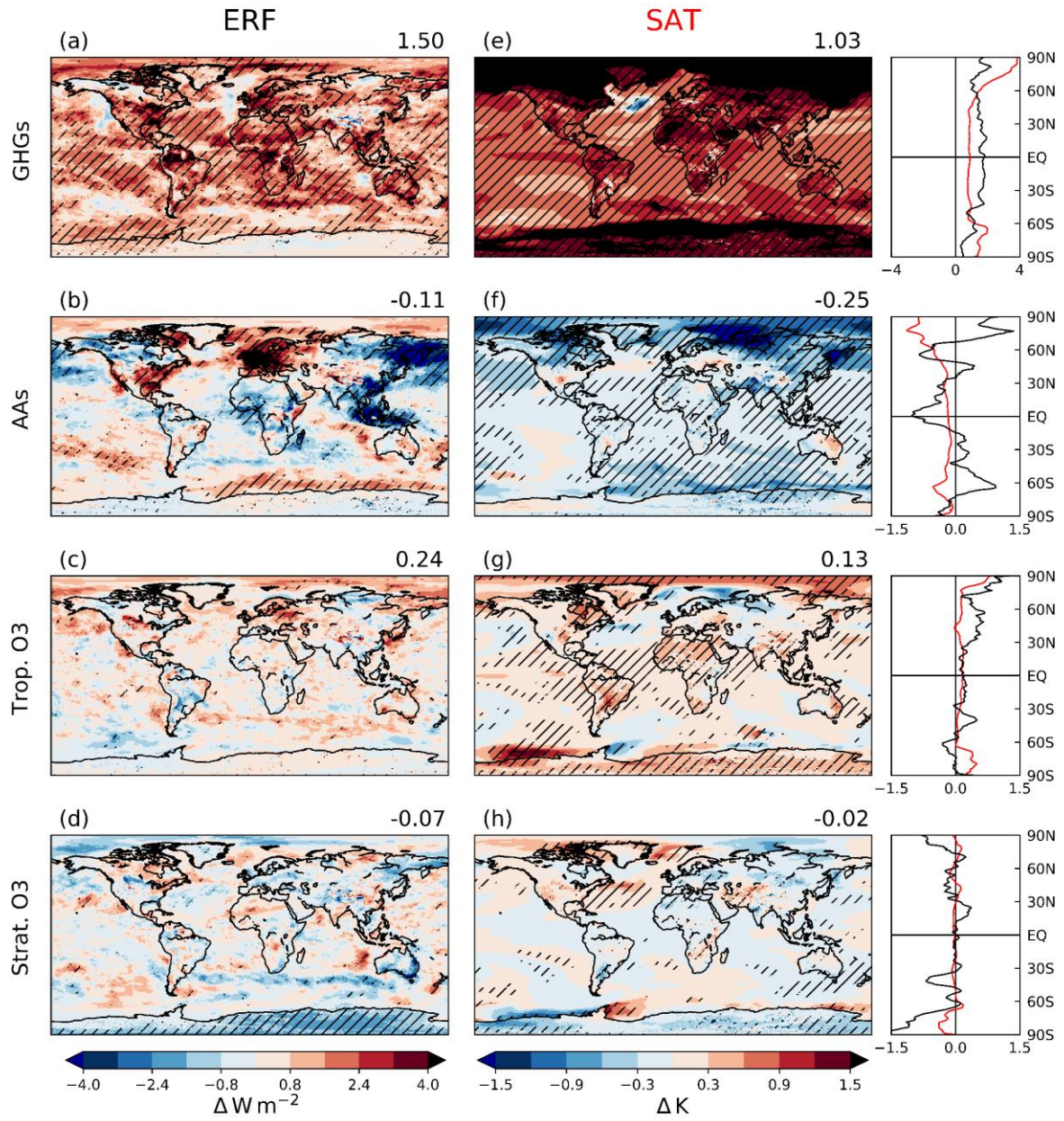

Figure 4 Spatial distribution of 2010 relative to 1970 (a-d) top-of-the-atmosphere effective radiative forcing (ERF) and (e-h) surface air temperature (SAT), in responses to changes in (a, e) greenhouse gases (GHGs), (b, f) anthropogenic aerosols (AAs), (c, g) tropospheric ozone increase (Trop. O_3) and (d, h) stratospheric ozone depletion (Strat. O_3). The right column shows the zonal mean changes (black for ERF and red for SAT); note the different x-axis scales between GHGs and others, as well as the different units between SAT (K) and ERF (W m^{-2}). Also see Figure S2 for the redrafted zonal mean temperature changes for comparison. Numbers on the top right of each panel are the area-weighted global mean values.

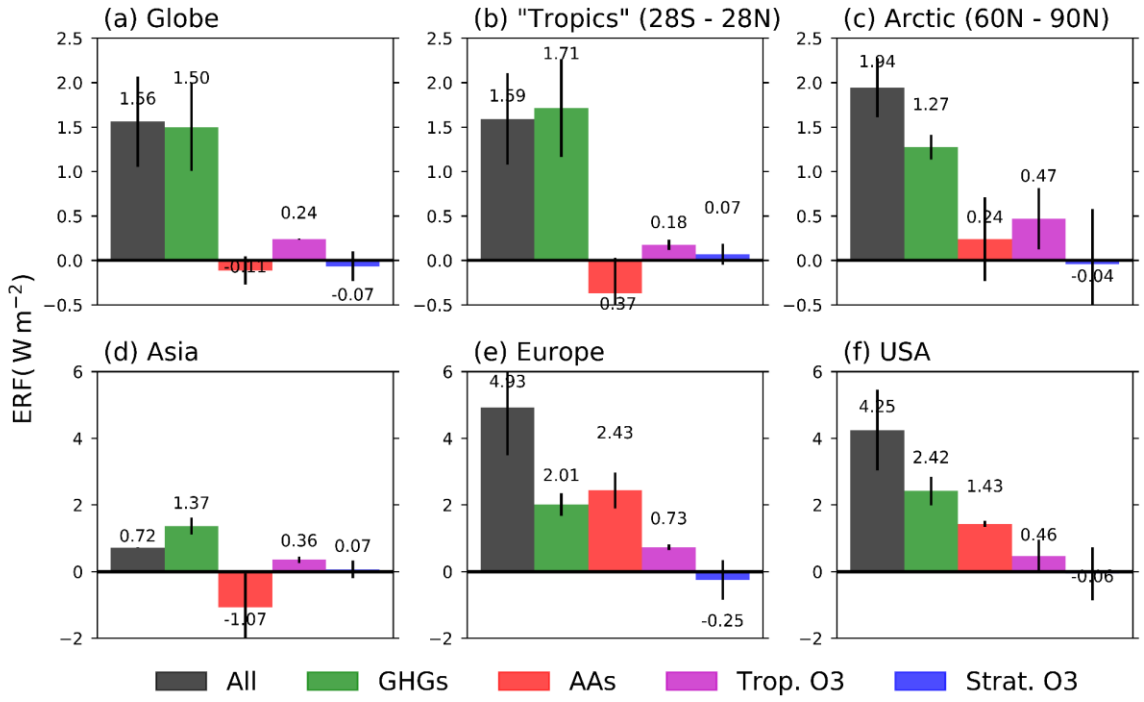

Figure 5 Area-weighted mean of 2010 relative to 1970 top-of-the-atmosphere ERF (W m^{-2}) over (a) global scale, (b) Tropical region (28°S-28°N), (c) Arctic (60°N-90°N), (d) Asia, (e) Europe and (f) USA. The total ERF (black) is resolved into those associated with each forcing agents: GHGs (green), AAs (red), Trop. O_3 (purple) and Strat. O_3 (blue). Error bars indicate the standard deviation spread.

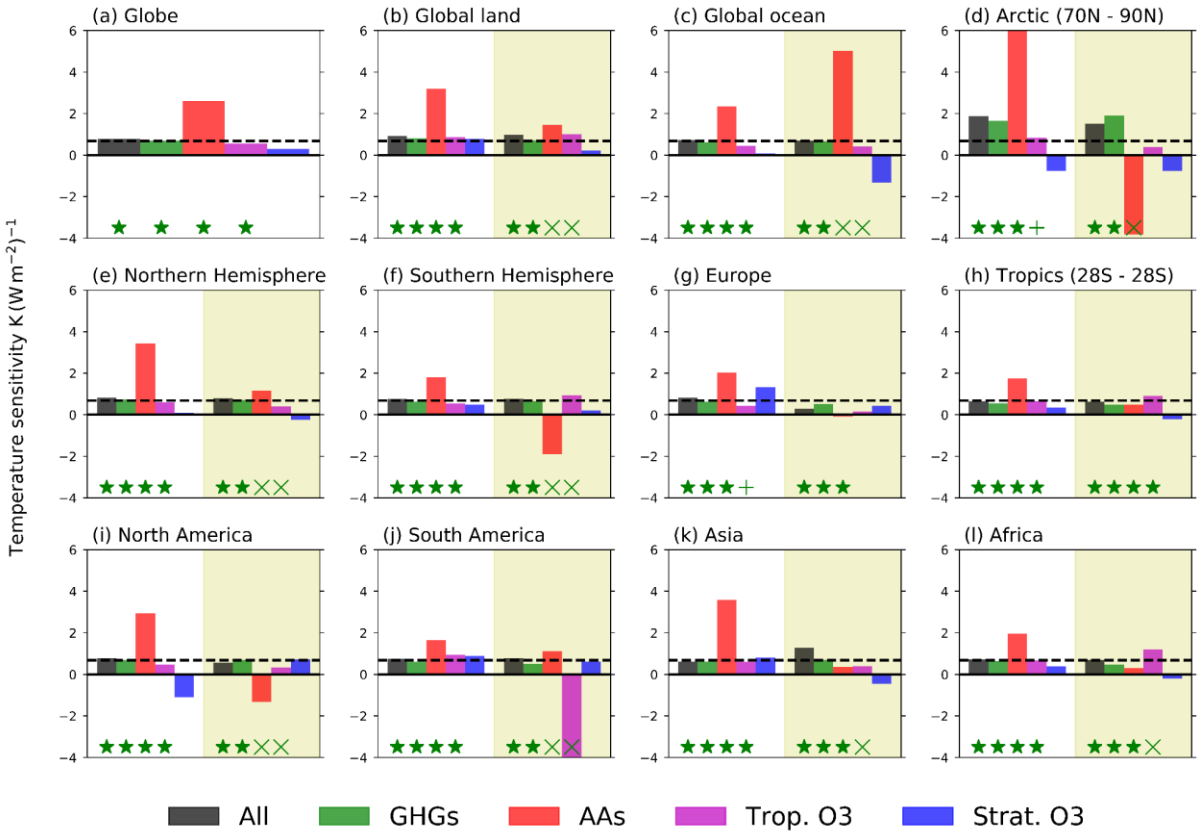

Figure 6 The sensitivity (K (W m^{-2})$^{-1}$) of area-weighted mean temperature responses per unit ERF from all forcings (black), GHGs (green), AAs (red), Trop. O_3 (purple) and Strat. O_3 (blue). The response is normalized by global (white background) and regional (yellow background) mean ERFs. The blue dashed lines indicate the global mean temperature response normalized by global GHG forcing (0.68 K (W m^{-2})$^{-1}$). The results are shown for (a) globe, (b) global land, (c) global ocean, (d) Arctic (70°-90°N), (e) Northern Hemisphere, (f) Southern Hemisphere, (g) Europe, (h) Tropics (28°S-28°N), (i) North America, (j) South America, (k) Asia and (l) Africa. Green stars denote that both global/regional mean ERF and temperature response are statistically significant (p-value <0.05, two-tailed student t-test), while green plus and cross denote, respectively, that only ERF or temperature response is statistically significant.

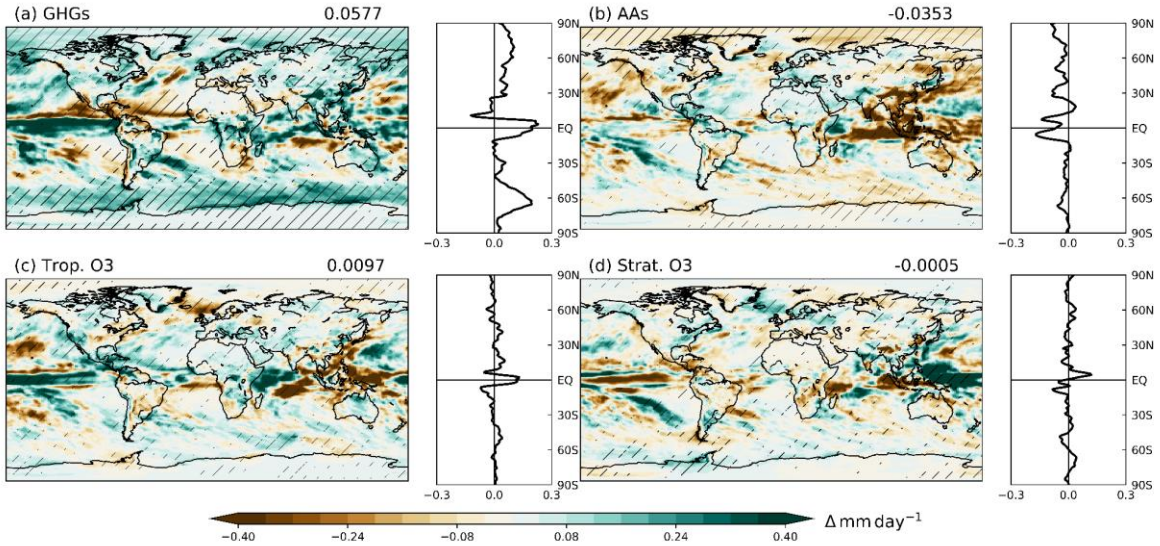

Figure 7 Spatial distribution and the zonal mean of precipitation changes, in response to 1970-2010 changes in (a) GHGs, (b) AAs (c) Trop. O_3 and (d) Strat. O_3. Numbers on the top right of each panel are the global mean values. Also see Figure S4 for the redrafted zonal mean precipitation changes for comparison.

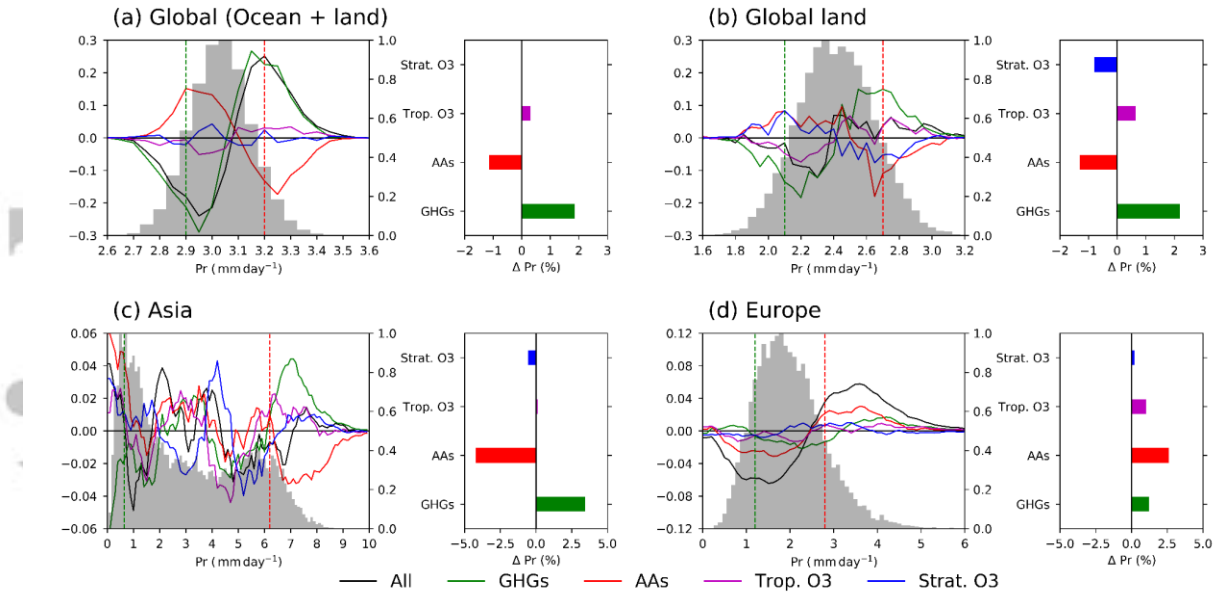

Figure 8 The 1970-2010 variations in the probability distribution (PDFs, curves, left axis) of area-weighted mean daily precipitation, as well as the shift of the mean value of the distribution in percent (bars, percent relative to 1970). The PDFs are calculated over bins with a size of 0.05 mm day^{-1} and then normalized by the peak frequency of the corresponding 1970 climatological distribution (grey histogram). The 10th and 90th percentiles of the climatological distribution are denoted by the green and red vertical dashed lines, respectively. Note for Asia and Europe, the variations in the probability distributions (curves) are merged into larger bins (0.5 mm day^{-1}) for legibility. Results are shown for (a) globe, (b) global land, (c) Asia and (d) Europe. The 1970-2010 total changes are resolved into each individual forcings: GHGs (green), AAs (red), Trop.O_3 (purple) and Strat.O_3 (blue).